

Cite this: *Chem. Sci.*, 2022, **13**, 4623

All publication charges for this article have been paid for by the Royal Society of Chemistry

Received 1st February 2022
Accepted 31st March 2022

DOI: 10.1039/d2sc00630h
rsc.li/chemical-science

Introduction

In 2018, the isolation of the aluminum(i) compound $K_2[Al(NON)]_2$, consisting of a three-coordinated Al supported by a dianionic, di(amido)dimethylxanthene-based $[NON]^{2-}$ ($NON = 4,5\text{-bis}(2,6\text{-diisopropylanilido})\text{-}2,7\text{-di-}tert\text{-butyl-}9,9\text{-dimethylxanthene}$) ligand, sanctioned a novel class of anionic Al(i) compounds, named the alumanyl anions (species **I**, Scheme 1).^{1,2} Shortly after this discovery, the family of alumanyl anions enlarged to include five additional members (species **II**, **III**, **IV**, **V** and **VI** in Scheme 1).³⁻⁷ Synthesis, structures and reactivity for this series of six alumanyl anions and their associated metal complexes were reviewed and reactions including nucleophilic substitution, oxidative addition, cycloaddition, reductions and oxidations were summarized, with special focus on the C–H and C–F activation, small molecules activation and the ring opening of aromatics.⁸

Metal–alumanyl complexes are of particular interest, since the electronic properties of alumanyl closely resemble those of carbenes, which represent a class of ubiquitous and extremely versatile ligands in coordination chemistry.⁹⁻¹³ Indeed, as

Unraveling differences in alumanyl and carbene coordination chemistry: bonding in gold complexes and reactivity with carbon dioxide[†]

Diego Sorbelli, *ab Leonardo Belpassi *b and Paola Belanzoni *ab

The electronic properties of alumanyl anions have been reported to be strictly related to those of carbenes, which are well-known to be easily tunable *via* selected structural modifications imposed on their backbone. Since peculiar reactivity of gold-alumanyl complexes towards carbon dioxide has been reported, leading to insertion of CO_2 into the Au–Al bond, in this work the electronic structure and reactivity of Au–Al complexes with different alumanyl scaffolds have been systematically studied and compared to carbene analogues. The analyses reveal that, instead, alumynils and carbenes display a very different behavior when bound to gold, with the alumynils forming an electron-sharing and weakly polarized Au–Al bond, which turns out to be poorly modulated by structural modifications of the ligand. The reactivity of gold–alumanyl complexes towards CO_2 shows, both qualitatively and quantitatively, similar reaction mechanisms, reflecting the scarce tunability of their electronic structure and bond nature. This work provides further insights and perspectives on the properties of the alumanyl anions and their behavior as coordination ligands.

shown in Fig. 1, in the most relevant frontier orbitals (FMO) manifold, both alumynils and singlet carbenes feature (i) a lone pair on the Al/C atom respectively, associated with their donating ability, which is responsible for their nucleophilic behavior and (ii) an empty p orbital (3p for Al and 2p for C), associated with their acceptor capability, which is, in turn, responsible for their electrophilicity.^{14,15}

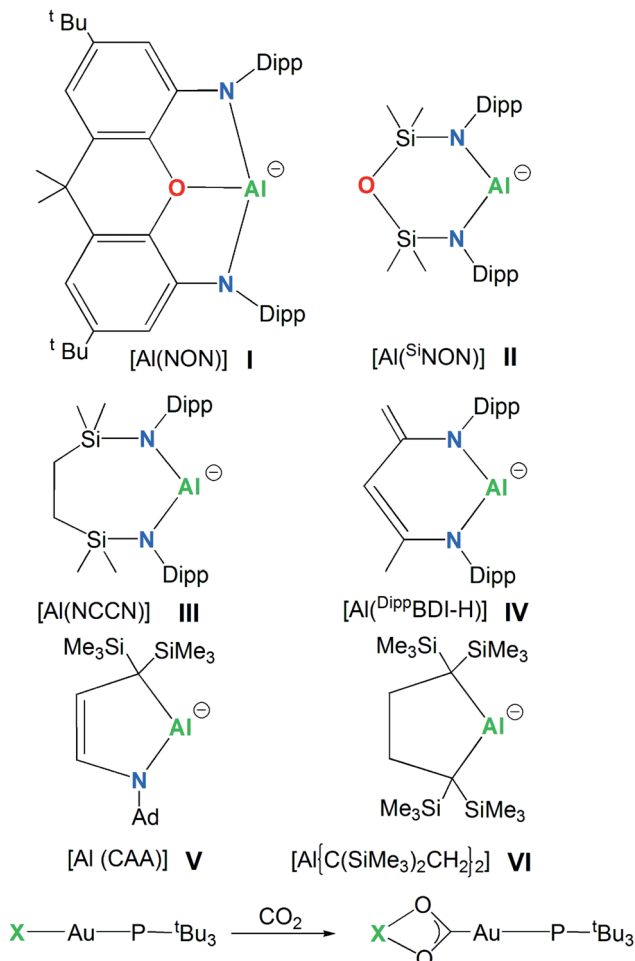
The electronic structure of carbenes is intimately related to their nucleophilic/eletrophilic behavior, with the stability of the HOMO, which allocates the lone pair, being an indicator of their nucleophilicity (the higher the HOMO energy, the more nucleophilic the carbene) and the stability of the LUMO, which can be ascribed to the empty 2p orbital of C, being a measure of their electrophilicity (the lower the LUMO energy, the more electrophilic the carbene).¹⁵ Another particularly interesting feature of carbenes is that their electronic properties can be sizably modulated by applying selected modifications on their structure.¹⁴⁻¹⁶ For instance, the nucleophilicity of carbenes can be enhanced by modifying the size of the ring, where, in the so-called Ring Expanded N-Heterocyclic carbenes (RENHCs),^{17,18} the wider N–C–N angle of six- and seven-membered NHCs corresponds to an increase of the p-character of the lone pair, which, in turn, destabilizes the HOMO and enhances its nucleophilic behavior.^{16,19} Analogously, as it has been reported for anti-Bredt carbenes,²⁰ a pyramidalized N substituent, due to a reduced N-to-C π -donation, is able to decrease the LUMO energy enhancing their electrophilicity. Additionally, the synthesis of cyclic (alkyl)(amino)carbenes²¹⁻²³ (CAACs) sanctioned the advent of a class of cyclic carbenes with enhanced

^aDepartment of Chemistry, Biology and Biotechnology, University of Perugia, Via Elce di Sotto, 8 – 06123, Perugia, Italy. E-mail: diegosorbelli00@gmail.com; paola.belanzoni@unipg.it

^bCNR Institute of Chemical Science and Technologies "Giulio Natta" (CNR-SCITEC), Via Elce di Sotto, 8 – 06123, Perugia, Italy. E-mail: leonardo.belpassi@cnr.it

† Electronic supplementary information (ESI) available. See DOI: [10.1039/d2sc00630h](https://doi.org/10.1039/d2sc00630h)





Scheme 1 Aluminyl anions studied here (species I–VI) and the CO_2 insertion reaction in their corresponding model gold complexes [$^t\text{Bu}_3\text{PAuX}$] ($\text{X} = \text{I}, \text{II}, \text{III}, \text{IV}, \text{V}$ and VI).

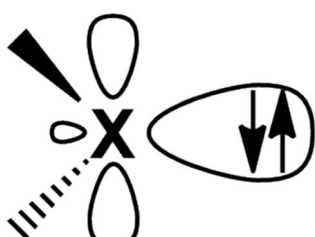


Fig. 1 Schematic representation of the lone pair and the vacant $2p/3p$ orbital on the C and Al atoms of carbenes and aluminyls, respectively.

electrophilicity (due to lowered N-to-C π -donation which induces a LUMO stabilization) and nucleophilicity (decreased electronegativity of one of the α -substituent which induces HOMO destabilization).^{19,21}

At a first sight, the analysis of the most relevant molecular orbitals (MOs) of the aluminyl anions **I**–**III** and **V**–**VI** in their monomeric form reported in ref. 8 revealed a qualitatively similar relationship between electronic effects and geometrical structure. Indeed, HOMO destabilization was found for the seven-membered **III** with respect to the six-membered **II** (as a consequence of the ring size) anion and for **V** and **VI** anions (due to the reduced electronegativity of the carbon α atoms). Similarly, the MO corresponding to the $3p$ empty orbital of Al (which, however, unlike carbenes, does not correspond to LUMO in all cases) is stabilized not only for CAAC-like aluminyls **V** and **VI** (due to reduced/absent π -donation towards Al) but also for **I**, for which, in addition to a small effect of the Al–O σ^* character (thus implying the existence of a bond between Al and the O atom of NON), the reduced N-to-Al π -donation is induced by geometrical restraints similarly to what happens for anti-Bredt carbenes. In addition to this, analogies between Arduengo-type carbenes and isoelectronic analogues with the group 13 elements (B, Al, Ga, In) have been also computationally previously predicted.²⁴

Notably, it has been extensively reported that the relationship between electronic properties and structure can be transferred to the features of the coordination bond in metal–NHC complexes. Particularly, in the case of gold(i)-NHC complexes, the Au–C bond can be described, according to the Dewar–Chatt–Duncanson (DCD) model, as consisting of a σ C-to-Au donation and a non-negligible Au \rightarrow C π back-donation^{10,25–30} and both components are found to be highly tunable with respect to the structural modifications discussed earlier.³⁰ Similar tuning has also been reported for the trans effect in gold(i)-alkynyl complexes.³¹

Analogous experimental and/or theoretical systematic studies assessing this relationship for metal–aluminyl complexes have been never reported to the best of our knowledge, despite the interesting and novel chemistry of metal–aluminyl compounds. In this regard, it was recently revealed that the gold complex of aluminyl anion **I**, the [$^t\text{Bu}_3\text{PAuAl}(\text{NON})$] complex, is surprisingly able to insert CO_2 into the Au–Al bond, leading to the [$^t\text{Bu}_3\text{PAuCO}_2\text{Al}(\text{NON})$] product with the CO_2 carbon atom coordinated to Au.³² Based on mechanistic and electronic structure analysis, we recently unraveled a bimetallic radical-like reactivity towards CO_2 , with the Au–Al bond acting as a nucleophilic site, consistently with an electron-sharing, weakly polarized Au–Al bond, which is also assisted by the electrophilic behavior of Al through its empty $3p_z$ orbital.³³

Within this framework, the Au–Al bond/reactivity relationship is certainly worth exploring to advance our knowledge on the nature of this new type of Au–Al bond and on its possible tuning through structural modifications of the aluminyl scaffold.

The aluminyl chemistry is currently widely studied and the number of aluminium nucleophiles is rapidly expanding.³⁴ However, the experimentally synthesized and characterized aluminyl nucleophiles depicted in Scheme 1 sufficiently differ each other from a structural point of view to our aim. Anion **I** is a three-coordinated Al species, anions **II** and **III** are two-coordinated Al species supported by bidentate six- and seven-



membered diamino ligands, $K_2[Al^{SiNON}]_2$ ($^{SiNON} = \{O(SiMe_2NDipp)\}_2\}$)³ and $K_2[Al(NCCN)]_2$ ($NCCN = \{CH_2SiMe_2-N(Dipp)\}_2$, Dipp = 2,6-iPr₂C₆H₃)⁴, respectively. Anion **IV** is a two-coordinated Al by the chelating β -diketiminato six-membered planar ligand, where a backbone Me group is deprotonated $K[Al^{(DippBDI-H)}]$ ($DippBDI-H = H_2C=C(N-Dipp)-C(H)=C(Me)-N-Dipp$)⁵. Substitution of nitrogen with carbon atoms leads to alkyl alumanyl anions (species **V** and **VI**, Scheme 1). Both compounds $[K(toluene)_2-Al\{(C(SiMe_3)_2CH_2\}_2]$ ⁶ and $[K(12\text{-crown-4})_2][Al(CAA)]$ ⁷ (CAA = cyclic alkyl amino = $\{C_2H_2-C(SiMe_3)_2NAd\}$, Ad = 1-adamantyl) feature 5-membered aluminium heterocycles, essentially differing by two carbon atoms (anion **VI**) vs. one carbon and one nitrogen atoms (anion **V**) as ligand donors in the ring.

In this work we investigate the features of the Au–Al bond in this series of gold–alumanyl complexes in close relationship with the Au–C bond in gold–carbene analogues. Although carbene homologues of **I–VI** have not been synthesized yet, at least to our knowledge, gold complexes bearing saturated six- and seven-membered RENHCs ligands have been reported previously.^{35,36} We also analyze the mechanism of the CO₂ insertion in the [^tBu₃PAuX] (X = alumanyl anions **I**, **II**, **III**, **IV**, **V** and **VI**, Scheme 1) complexes in tight connection with their electronic structure, within the interpretative framework provided in ref. 33. To directly compare the alumanyl anions **I–VI** bonding properties towards Au and the reactivity of the corresponding complexes with carbon dioxide, a common [^tBu₃PAu]⁺ metal fragment has been selected (Scheme 1).

We unravel that actually alumynils show a different behavior with respect to carbenes as gold ligands: a highly-covalent, weakly polar Au–Al bond is formed in all gold–alumanyl complexes, revealing a different nature with respect to the Au–C bond in gold–carbene analogues, which is mainly dative. As a consequence, the possibility of tuning the features of the Au–Al bond by imposing structural modifications on the alumanyl is highly reduced. As a result of the scarce tunability of their electronic structures, the six complexes under study are demonstrated to show no remarkable differences when reacting with CO₂, favoring in all cases the formation of similarly stable [^tBu₃PAuCO₂X] insertion products.

Results and discussion

Comparative analysis of the Au–Al bond

By relying on the use of Energy Decomposition Analysis (EDA),^{37,38} and Charge Displacement (CD) analysis,^{39–41} combined with the ETS-NOCV (Extended Transition State – Natural Orbitals for Chemical Valence)⁴² approach, we investigate in detail the features of the bond between the gold and alumanyl fragments within a quantitative and comparative framework, to unravel if and how such features can be modulated by the structural modifications imposed by the alumanyl ligand scaffold.

Firstly, based on the computational protocol reported in ref. 43 and 44, we carry out a comparative EDA using differently charged fragments (*i.e.* [^tBu₃PAu]^{+/0/−}–[X]^{−/0/+}) in order to assess which fragmentation scheme is the most suitable for the

Table 1 Orbital interaction energies (ΔE_{oi}^{k}) and charge transfer (CT^k) associated with the first three NOCV deformation densities for the interaction between neutral doublet [^tBu₃PAu][·] and [X][·] (X = **I–VI**) for complexes [^tBu₃PAuX]. The overall ΔE_{oi} and ΔE values from the EDA are also reported. Values for [^tBu₃PAuI] and [^tBu₃PAuII] are taken from ref. 33 and 45, respectively

X	I	II	III	IV	V	VI
CT ^{1α}	−0.272	−0.312	−0.284	−0.325	−0.287	−0.298
$\Delta E_{oi}^{1\alpha}$	−32.7	−33.1	−34.3	−43.6	−33.9	−34.6
CT ^{1β}	0.299	0.299	0.304	0.300	0.304	0.307
$\Delta E_{oi}^{1\beta}$	−24.5	−23.4	−24.0	−23.6	−23.7	−23.8
CT ¹	0.027	−0.013	0.020	−0.025	0.017	0.009
ΔE_{oi}^{2}	−4.3	−4.3	−4.4	−4.2	−4.2	−4.7
CT ²	−0.030	−0.038	−0.029	−0.020	−0.024	−0.032
ΔE_{oi}^{3}	−3.3	−3.6	−3.5	−3.4	−3.8	−3.5
CT ³	−0.018	−0.027	−0.014	−0.015	−0.020	−0.020
ΔE_{oi}	−71.5	−70.9	−73.4	−84.6	−72.1	−72.8
ΔE	−87.6	−87.1	−84.7	−90.7	−83.5	−83.3

description of the Au–Al bond. This approach, coherently with the previously reported results for [^tBu₃PAu–I] and [^tBu₃PAu–II],^{33,45} reveals that in all the cases the best fragmentation scheme is in terms of neutral doublet [^tBu₃PAu][·] and [X][·] fragments (see Tables S1–S4† in the ESI for the results).

Next, we combine CD and ETS-NOCV approaches for analyzing the Au–Al bond in the complexes under study. The numerical results of the CD-NOCV analysis are reported in Table 1, with the CD-NOCV curves associated with the $\Delta\rho'_1$

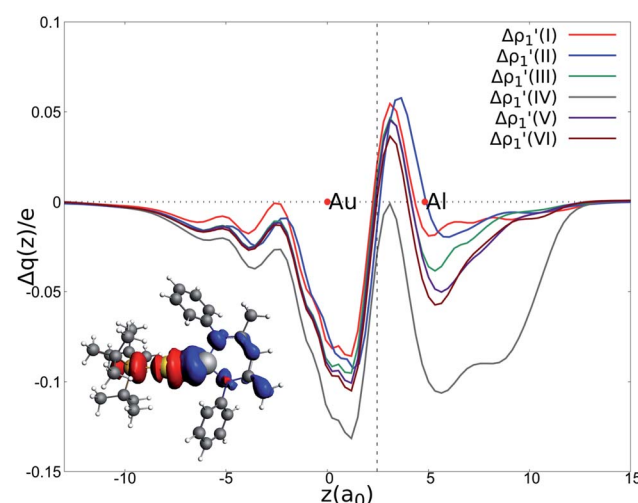


Fig. 2 Charge Displacement (CD-NOCV) curves associated with the $\Delta\rho'_1$ NOCV deformation density for the interaction between doublet [^tBu₃PAu][·] and [X][·] (X = **I–VI**) fragments for complexes [^tBu₃PAuX]. Red dots indicate the average position of the nuclei along the z axis. The black dashed line indicates the average position of the isodensity boundary. Positive (negative) values of the curve indicate right-to-left (left-to-right) charge transfer. *Inset:* isodensity surfaces associated with the $\Delta\rho'_{1\alpha}$ NOCV deformation density for complex [^tBu₃PAuIV]. Charge flux is red-to-blue. Isodensity value is 1 me a₀^{−3}. Results for [^tBu₃PAuI] and [^tBu₃PAuII] are taken and adapted from ref. 33 and 45, respectively.

NOCV deformation density depicted in Fig. 2. All the curves associated with the different NOCV deformation densities ($\Delta\rho'_{1\alpha}$, $\Delta\rho'_{1\beta}$, $\Delta\rho'_{2}$ and $\Delta\rho'_{3}$) and the corresponding isosurfaces are reported in the ESI (Fig. S1–S5†).

The results of the CD-NOCV analysis unequivocally point out a clear outcome concerning the nature of the Au–Al bond: structural modifications on the alumanyl scaffold appear to be not relevant for tuning the features of the Au–Al bond.

In detail, in complexes $[^t\text{Bu}_3\text{PAuIII}]$ – $[^t\text{Bu}_3\text{PAuVI}]$, the Au–Al bond can be envisaged to be mainly consisting of two opposite charge transfers (CTs), namely an Al-to-Au CT ($\Delta\rho'_{1\beta}$) and an Au-to-Al charge flux ($\Delta\rho'_{1\alpha}$), as found for $[^t\text{Bu}_3\text{PAuI}]$ and $[^t\text{Bu}_3\text{PAuII}]$ in ref. 33 and 45, respectively. On a quantitative ground, the former is surprisingly very similar for all the complexes. Indeed, the extent of the Al-to-Au charge flux is practically identical for all the complexes (the corresponding CT^{1β} values vary in the 0.299–0.307e range, Table 1) and, consistently, the associated stabilizing orbital interaction $\Delta E_{\text{oi}}^{1\beta}$ varies in a very narrow range (1.1 kcal mol^{−1}, Table 1). This result is surprising since it suggests that the donor ability of the alumanyl moiety, despite the structural differences between anions **I**–**VI**, remains substantially unaltered.

Similarly, the Au-to-Al charge flux appears also to be only marginally affected by such modifications. Although the Au-to-Al charge transfer varies in a slightly wider range for complexes $[^t\text{Bu}_3\text{PAuI}]$ – $[^t\text{Bu}_3\text{PAuIII}]$ and $[^t\text{Bu}_3\text{PAuV}]$ – $[^t\text{Bu}_3\text{PAuVI}]$ (CT^{1α}–0.272/–0.312e), the associated $\Delta E_{\text{oi}}^{1\alpha}$ values clearly demonstrate that, overall, no significant influence of the alumanyl ligand is detected along the series ($\Delta E_{\text{oi}}^{1\alpha}$ varies in a range of 1.9 kcal mol^{−1} for these complexes). Analogously, the overall interaction energies ΔE in this series vary in a particularly narrow range (−87.6/–83.3 kcal mol^{−1}, see ref. 33, 45 and Tables S1–S4† in the ESI). This is again an outstanding result, particularly because the acceptor ability (electrophilicity) of the group 13 alumanyl anion has been recently demonstrated to be a crucial factor in these complexes for determining the degree of covalency of the Au–X bond and potentially their reactivity towards CO₂.³³ Despite this homogeneity, some differences can be observed for complex $[^t\text{Bu}_3\text{PAuIV}]$. As it can be envisioned from the data in Table 1 and from the CD-NOCV curve in Fig. 2, the $[\text{Al}^{(\text{DippBDI-H}')}]$ fragment seems to have an enhanced ability of accepting charge from gold, with both increased CT^{1α} and $\Delta E_{\text{oi}}^{1\alpha}$ values (−0.325e and −43.6 kcal mol^{−1}, respectively). Upon inspection of the isodensity surface related to the $\Delta E_{\text{oi}}^{1\alpha}$ NOCV deformation density (see inset of Fig. 2), it is clear that this different behavior in $[^t\text{Bu}_3\text{PAuIV}]$ is determined by the planarity of the $[\text{Al}^{(\text{DippBDI-H}')}]$ anion, which, as clearly shown in the isodensity picture, is responsible for an hyperconjugation interaction, where the Au–Al σ bond formally interacts with the π-system of the planar $[\text{Al}^{(\text{DippBDI-H}')}]$ ^{2−} backbone.

Interestingly, we should note that complex $[^t\text{Bu}_3\text{PAuI}]$, in which the $[\text{Al}(\text{NON}')]$ is the only alumanyl bearing a tri-coordinated Al in the series, is very much analogous to the di-coordinated Al alumynyls $[^t\text{Bu}_3\text{PAuII}]$ and $[^t\text{Bu}_3\text{PAuIII}]$, thus suggesting that the oxygen atom of NON has not a direct effect on the Au–Al bond. Indeed, the isodensity surfaces of the $\Delta\rho'_{1\alpha}$, $\Delta\rho'_{1\beta}$, $\Delta\rho'_{2}$ and $\Delta\rho'_{3}$ NOCV deformation densities

(Fig. S1–S4†) do not show any depletion/accumulation pattern involving the NON oxygen atom, thus ruling out a significant electronic influence due to the existence of a possible Al–O bond.

Overall, these analogies and differences are well explained by the CD-NOCV curves in Fig. 2 and the associated CT values of the total $\Delta\rho'_1$ component. As it can be seen, most of the net curves practically overlap (and have values close to zero) in the region of the Au–Al bond, clearly indicating an overall electron-rich, highly covalent and weakly polarized Au–Al bond, as also demonstrated by the very small values of net CT (Table 1). Yet again, complex $[^t\text{Bu}_3\text{PAuIV}]$ is an outlier in this series, as it can be envisaged by the corresponding CD-NOCV curve, which suggests a slightly more significant Au(δ⁺)-Al(δ[−]) polarization of the bond, consistently with the results discussed earlier.

Analogously to $[^t\text{Bu}_3\text{PAuI}]$ and $[^t\text{Bu}_3\text{PAuII}]$, complexes $[^t\text{Bu}_3\text{PAuIII}]$ – $[^t\text{Bu}_3\text{PAuVI}]$ have two dative π back-donation components, which, as demonstrated by the CT values reported in Table 1 and by the CD-NOCV curves shown in Fig. S5,† are very small in magnitude and do not display significant modulation upon variation of the alumanyl moiety.

Alumynyls/carbenes Au–Al/Au–C bond comparison

Based on the results illustrated in the previous section, it appears that the main features of the bond between gold and alumynyl fragments are hardly affected by the different structural modifications at the alumynyl site, thus highlighting substantial differences with respect to their carbene counterparts. In light of this finding, here we quantitatively assess the carbene/alumynyl ligand relationship.

Firstly, to discuss in more detail the results reported in ref. 8 concerning the similarities between carbenes and alumynyls in terms of frontier molecular orbitals (FMOs), we optimize isolated anions **I**–**VI** and their carbene analogues **Y** (**Y** = C(NON'), C(^{Si}NON'), C(NCCN'), C(^{Dipp}BDI-H'), C(CAA'), C({C(SiH₃)₂CH₂})₂), labeled as **I**^C–**VI**^C in the order). This allows to quantitatively compare the trends observed for the most relevant FMOs. Their FMO energies are reported in Fig. S6 in the ESI.† As it can be clearly envisaged by the FMO energies along the two series of carbenes and alumynyls, respectively, while qualitatively the two trends are generally alike (corroborating the similarities discussed in ref. 8) from a quantitative perspective we readily realize that the electronic properties of the alumynyls appear to be less responsive to the structural differences. Indeed, for the lone pair orbital (HOMO), in the case of carbenes its energy varies in a much wider range with respect to alumynyls (1.1 vs. 0.4 eV, respectively) and a similar pattern is observed for the MO corresponding to the vacant 2p/3p orbital of C/Al (1.2 eV vs. 0.6 eV, respectively).

Despite the FMO-based analysis suggests some differences between isolated alumynyls and carbenes, our aim is to assess properly and quantitatively an alumynyls/carbenes comparison as coordination ligands. We decided to study, by relying on the same EDA-CD-NOCV-based protocol used in the previous section, the features of the Au–C bond in the six cationic gold-carbene complexes $[^t\text{Bu}_3\text{PAuY}]^+$, which represent the



analogues of the [^tBu₃PAuX] complexes object of this study. The optimized structures of the [^tBu₃PAuY]⁺ complexes are depicted in Fig. S7 in the ESI,† and they are qualitatively very similar to those of their alumanyl counterparts.

Firstly, we identify which fragments describe the Au–C bond best, *i.e.* closed-shell [^tBu₃PAu]⁺–[Y] or doublet open-shell [^tBu₃PAu]⁺–[Y]⁺ fragments. This analysis is performed by using the EDA approach on both fragmentation schemes, and the results are reported in Table S5 in the ESI.† In contrast to their alumanyl counterparts, the interaction between gold and carbene fragments, as expected, is best described by closed-shell [^tBu₃PAu]⁺–[Y] fragments in all cases, as demonstrated by the less stabilizing orbital interaction (which is the indicator for the most suitable fragmentation scheme)^{43,44} for the closed-shell fragments.

This different fragmentation scheme suggests that the Au–C bond has probably a prevailing dative character and this can be quantitatively inferred by the results of the CD-NOCV analysis of the Au–C bond. The most relevant results are reported in Tables 2 and 3. The complete results can be found in Table S6, Fig. S8 and S9 in the ESI.†

The CD-NOCV results unequivocally depict the Au–C bond in complexes [^tBu₃PAuI^C]⁺–[^tBu₃PAuVI^C]⁺ as a “classical” metal–ligand coordination bond, with the main bond components that can be described within the framework of the Dewar–Chatt–Duncanson model. Indeed, consistently with the results reported in the literature for the Au(I)–NHC bond,^{30,46} the main

and first NOCV component is, in all the cases, a C-to-Au charge transfer of σ symmetry that can be envisaged as a σ donation ($\Delta\rho'_1$). Additionally, a gold-to-carbon π back-donation component parallel to the Au–N–C–N plane of significant extent can be recognized for all the complexes ($\Delta\rho'_2$). Finally, two additional minor dative components (namely a σ back-donation and a perpendicular π back-donation) are found for all complexes (see Table S6† for the corresponding CT and ΔE_{oi}^k values), coherently with previous literature results.^{30,46}

Since Al and C belong to both different groups and periods in the periodic table one may ask if the interplay between dative and electron-sharing nature bonds with gold could be influenced by the change along the group or the period. From the results we recently reported on a comparative analysis within the same framework of gold-alumanyl, -gallyl and -indyl complexes, we unraveled that, although the Au(δ^+)-X(δ^-) polarization increases on descending along group 13, the Au–X bond (X = Al, Ga, In) is in all cases best described as an electron-sharing bond with different degrees of polarization,⁴⁵ thus implying that the bond nature (and the electronic structure of the complexes) is mainly driven by a group effect. This is also confirmed by carrying out a comparative EDA using different fragmentation schemes on the boryl analogue of complex with VI (VI^B) and the silylene analogue of VI^C (VI^{Si}) as test cases (Tables S7 and S8 in the ESI†). The analysis reveals a predominant Au–B electron-sharing character for complex with VI^B and a dative Au–Si bond for complex with VI^{Si}. Therefore, the electronic structure (and the gold–ligand bond nature) differences in the alumanyl *versus* carbene complexes can be inferred to be mainly dictated by a group factor (with group 14 ligand favoring dative and group 13 ligand favoring electron-sharing type bonds with gold), rather than by a period (2nd *versus* 3rd) effect.

From a quantitative perspective, structural modifications of the carbenes and aluminyls scaffolds appear to have different effect on the Au–X bond in terms of tunability. Comparison between the trends of the CD-NOCV results along the series of carbenes (see Table 2) and aluminyls (see Table 1) clearly points out that the Au–C bond is modulated more efficiently with respect to the Au–Al bond.

In detail, the C-to-Au σ donation in carbene complexes appears to have a similar nature with respect to the Al-to-Au CT ($\Delta\rho'_{1B}$) in alumanyl complexes, since they both reflect the donor power of the alumanyl/carbene ligand (see the very similar related isosurfaces in Fig. S9†). However, these two components (the donor ability) display a different degree of variability along the corresponding series. We can quantitatively infer the degree of variability within each series by relying on the relative percentage variation values ε_1 associated with ΔE_{oi}^{1B} and ΔE_{oi}^1 for aluminyls and carbenes, respectively (we resort to the use of this quantity to make the comparison as meaningful as possible). As shown in Table 3, ε_1 values vary in a much narrower range for aluminyls with respect to carbenes (0.0/2.7% *vs.* 0.0/8.6%, respectively), thus indicating an enhanced modularity of the Au–C bond. A similar pattern is observed for the π back-donation component, for which relative percentage variation values (ε_2) clearly underline that this bond component is highly tunable upon structural modifications of the carbene

Table 2 Orbital interaction energies (ΔE_{oi}^k) and charge transfer (CT^k) associated with the first two NOCV deformation densities ($\Delta\rho'_1$ and $\Delta\rho'_2$) for the interaction between closed-shell [^tBu₃PAu]⁺ and [Y] fragments Y I^C–VI^C) for complexes [^tBu₃PAuI^C]⁺–[^tBu₃PAuVI^C]⁺. Energies are reported in kcal mol^{–1}, CT values are reported in electrons

X	I ^C	II ^C	III ^C	IV ^C	V ^C	VI ^C
ΔE_{oi}^1	–46.6	–49.8	–50.6	–46.6	–47.6	–49.6
CT ¹	0.364	0.381	0.390	0.358	0.360	0.382
ΔE_{oi}^2	–9.7	–8.3	–8.6	–9.0	–9.9	–11.9
CT ²	–0.057	–0.057	–0.062	–0.056	–0.048	–0.097

Table 3 Percentage variation ($\varepsilon_1 = [(\Delta E_{oi}^{1B} - \Delta E_{oi}^{1B\text{ref}})/\Delta E_{oi}^{1B\text{ref}}] \times 100$; $\varepsilon_2 = [(\Delta E_{oi}^2 - \Delta E_{oi}^{2\text{ref}})/\Delta E_{oi}^{2\text{ref}}] \times 100$) with respect to a reference value (values for I and I^C) of the orbital interaction associated to ΔE_{oi}^{1B} and ΔE_{oi}^2 for complexes [^tBu₃PAuI]–[^tBu₃PAuVI] and ΔE_{oi}^1 and ΔE_{oi}^2 for complexes [^tBu₃PAuI^C]⁺–[^tBu₃PAuVI^C]⁺

	ε_1		ε_2	
	Alumanyl	Carbene	Alumanyl	Carbene
I/I ^C	0.0	0.0	0.0	0.0
II/II ^C	0.0	6.9	0.0	–14.4
III/III ^C	1.7	8.6	2.3	–11.3
IV/IV ^C	0.3	0.0	2.3	–7.2
V/V ^C	1.7	2.1	2.3	2.1
VI/VI ^C	2.7	6.4	9.3	22.7



ligand (ε_2 varies in the $-14.4/22.7\%$ range). Conversely, also in agreement with the energetic trends observed for the FMOs of the isolated aluminyls, the degree of tunability is highly reduced in the case of aluminyls, with ε_2 varying in a much narrower range ($0.0/9.3\%$).

The evaluation of the strength and basicity of the lone pair of the **I–VI** and **I^C–VI^C** ligands also gives an idea of the different nature of these species.⁴⁵ On the basis of the gas phase proton affinity and the corresponding HOMO energy and composition properties, the aluminyls emerge as more reactive and basic ligands than carbenes (proton affinities in the $-349.6/-362.1$ kcal mol⁻¹ range for aluminyls and $-267.9/-301.3$ kcal mol⁻¹ range for carbenes, see Table S9 in the ESI[†]), as expected. However, whereas for carbenes the proton affinities span a range of 33.4 kcal mol⁻¹, for aluminyls they span a much more reduced range (12.5 kcal mol⁻¹), thus suggesting once again a reduced tunability of aluminyls upon ligand scaffold change. The peculiarity of the aluminyl ligands lone pair with respect to that of carbenes is strikingly evident by inspection of the isodensity pictures of the corresponding HOMOs, depicted in Fig. 3.

The aluminyl lone pair HOMO is very diffuse, mainly centred at the Al site, and it is poorly delocalized on the ligand, whereas the carbenes lone pair HOMO is much less diffuse and delocalizes over the ligand scaffold to a greater extent (for HOMOs atomic composition and energy see Table S9 in the ESI[†]), which explains why the structure of the ligands represents a control factor on their electronic properties, while such control is much reduced in the case of aluminyls.

This comparative analysis clarifies that, despite being isoelectronic and isolobal, aluminyls and carbenes display a very different behavior as coordination ligands, with the highly covalent Au–Al bond being poorly tunable upon structural modifications of the aluminyl. In the following section we

will discuss the impact of such reduced tunability of the bond in the reaction of complexes [^tBu₃PAuI]–[^tBu₃PAuVI] with CO₂.

Mechanistic study and electronic structure/reactivity relationship

The free energy profiles for the CO₂ insertion into the Au–Al bond in the [^tBu₃PAuX] (X = **I**, **II**, **III**, **IV**, **V** and **VI**) complexes have been calculated using the same computational setup as that in ref. 33 and 45 (see Computational details section) for a consistent comparison with the gold-aluminyl [^tBu₃PAuI] and [^tBu₃PAuII] complex results. They are compared in Fig. 4. Optimized structures of all the compounds and corresponding reactant complexes (RC), transition states (TSI and TSII), intermediates (INT) and product complexes (PC) are reported in the ESI (Fig. S10–S15[†]).

The reaction profiles in Fig. 4 are qualitatively very similar. In the first step, the nucleophilic attack to the CO₂ carbon atom by the Au–Al bond has a comparatively low activation free energy barrier, in the range 0.5–10.9 kcal mol⁻¹. In absolute value, the six TSIs lie above the corresponding separated reactants in the range 16.2–9.3 kcal mol⁻¹. Structures of transition states TSI for all the [^tBu₃PAuX] (X = **I**, **II**, **III**, **IV**, **V**, **VI**) complexes are sketched with selected geometrical parameters in Fig. 5.

At the TSI geometry, a very similar bending of CO₂ (160.0–163.4°) and asymmetry between the two C–O bonds (1.169/1.176 vs. 1.199/1.205) can be observed for complexes with **II**, **III**, **IV**, **V** and **VI** anions, whereas both CO₂ bending (146.3°), C–O asymmetry and elongation (1.203 vs. 1.216) are more pronounced for **I**. Interestingly, we recently reported that [^tBu₃PAuI] features a peculiar topology of the potential energy surface (PES) around TSI which is very flat, leading to locate an almost degenerate TSI structure where the CO₂ bending is 159.5° and C–O asymmetry is 1.175/1.199 Å, with an oxygen atom of CO₂ at 2.314 Å distance from Al, which is completely in line with all the other TSI

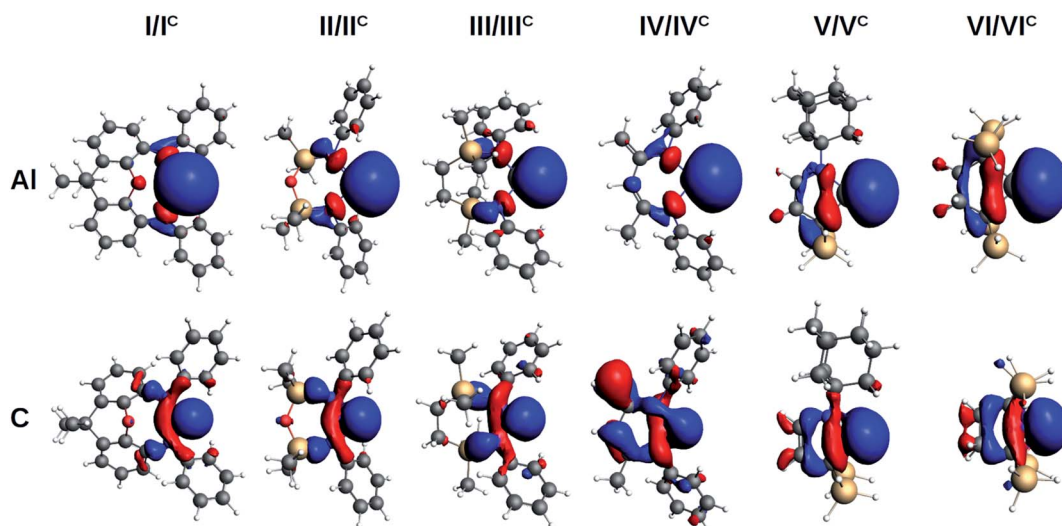


Fig. 3 Isosurfaces of the HOMO of aluminyls **I–VI** (first row) and carbenes **I^C–VI^C** (second row). Isovalue for all surfaces is 30 me a₀⁻³.



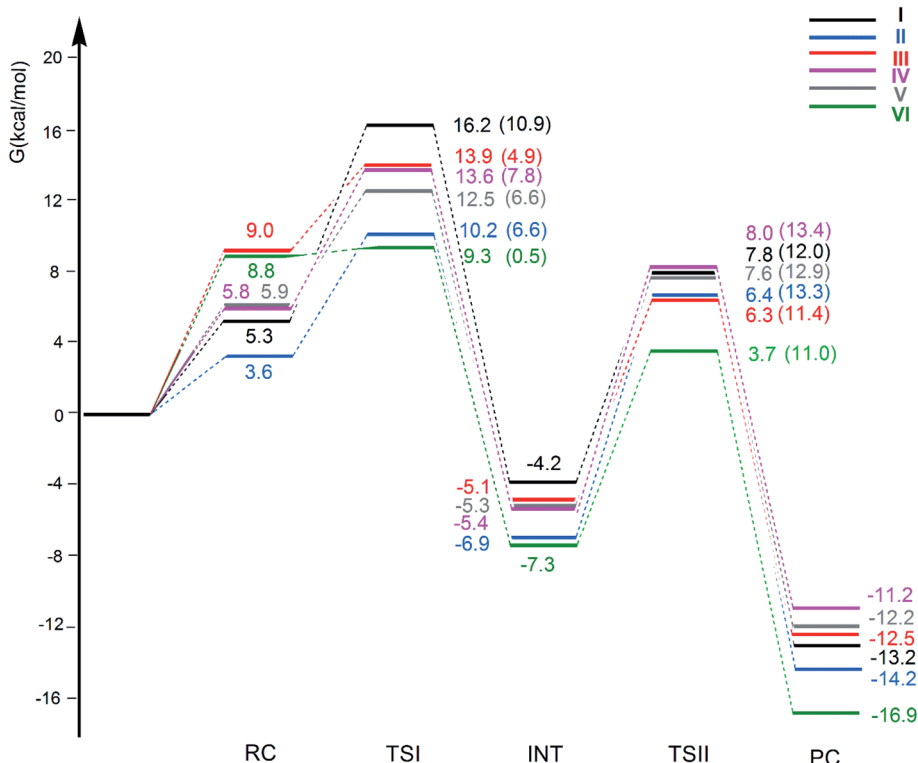


Fig. 4 Free energy reaction profile for the CO_2 insertion into the Au–Al bond in the $[\text{tBu}_3\text{PAuAl}(\text{NON}')]$ (I, black lines), $[\text{tBu}_3\text{PAuAl}(\text{S}^{\text{I}}\text{NON}')]$ (II, blue lines), $[\text{tBu}_3\text{PAuAl}(\text{NCCN}')]$ (III, red lines), $[\text{tBu}_3\text{PAuAl}(\text{DiPPBDI}-\text{H}')]$ (IV, violet lines), $[\text{tBu}_3\text{PAuAl}(\text{CAA}')]$ (V, grey lines) and $[\text{tBu}_3\text{PAuAl}(\text{C}(\text{SiH}_3)_2\text{CH}_2)_2]$ (VI, green lines) complexes. ΔG values refer to the energy of the separated reactants taken as zero. Activation free energy barriers are reported in parentheses. The results for $[\text{tBu}_3\text{PAuI}]$ and $[\text{tBu}_3\text{PAuII}]$ have been taken and adapted from ref. 33 and 45.

structures.⁴⁵ It is interesting to observe that the free energies of TSIs (and the corresponding ΔG^\ddagger values) do not correlate with the CO_2 bending, *i.e.* the free energy barrier range (10.9–0.5 kcal mol^{−1}) corresponds to the same CO_2 bending, which is

around 160° for all the complexes. This result is in full agreement with the finding in ref. 45 that carbon dioxide bending is not a good indicator of its activation.

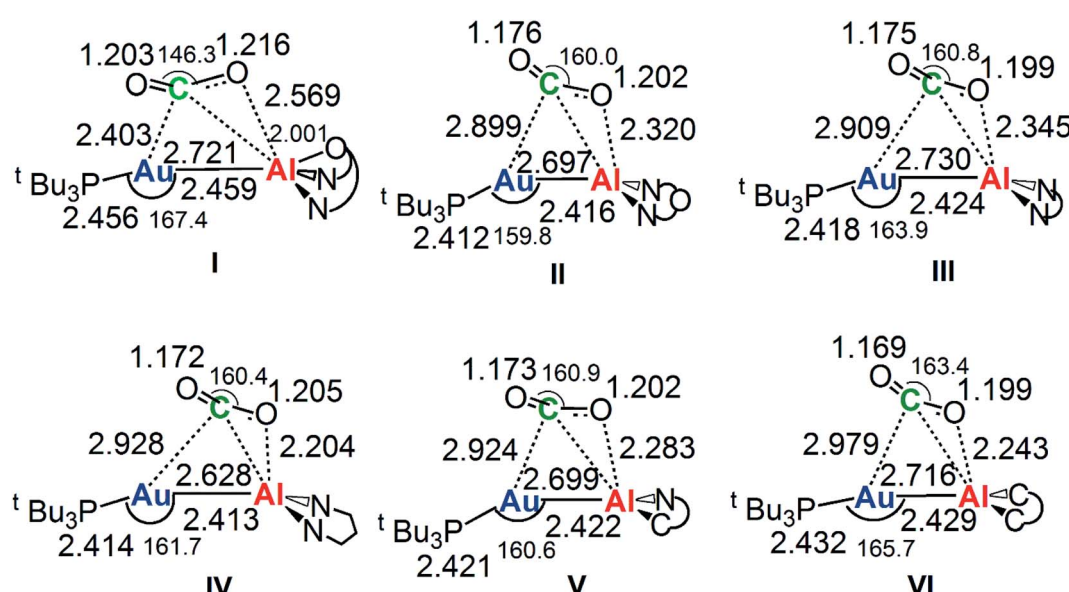


Fig. 5 Selected interatomic distances (in Å) and bond angles (degrees) are given with the sketched TSI structures of $[\text{tBu}_3\text{PAuX}]$ ($\text{X} = \text{I}, \text{II}, \text{III}, \text{IV}, \text{V}, \text{VI}$) complexes. The results for $[\text{tBu}_3\text{PAuI}]$ and $[\text{tBu}_3\text{PAuII}]$ have been taken and adapted from ref. 33 and 45.

Formation of intermediate INT leads to a four-membered (Au–C–O–Al) cyclic structure for all the complexes, with an Au–Al bond slightly larger for $[^t\text{Bu}_3\text{PAuI}]$ (2.623 Å vs. 2.602–2.572 Å, respectively) and a slightly higher stabilization (20.4 kcal mol^{−1} vs. 19.0–16.6 kcal mol^{−1}, respectively) with respect to complexes with **II**, **III**, **IV**, **V** and **VI** aluminyls. The CO₂ bending and asymmetry between the two C–O bonds is very comparable in all the systems (see Fig. S10–S15†).

The small differences observed in the first step of the reaction path can be well rationalized by relying on the Activation Strain Model (ASM),^{47–49} which decomposes the energy along the reaction path in two contributions: one arising from the interaction between the fragments ($\Delta\Delta E_{\text{int}}$) and the other representing the distortion of the interacting fragment from their relaxed geometry to their in-adduct configuration ($\Delta\Delta E_{\text{dist}}$, see the Methodology section in the ESI† for a brief description of the approach). The numerical results of the ASM approach for complexes $[^t\text{Bu}_3\text{PAuI}]$ – $[^t\text{Bu}_3\text{PAuVI}]$ are reported in Tables S10–S11 in the ESI† whereas the related Activation Strain diagrams (ASD) are depicted in Fig. 6.

As shown in Fig. 6a, most complexes feature similar electronic activation barriers involving TSI and similar stabilization extent of the intermediate INT. In particular, for complexes $[^t\text{Bu}_3\text{PAuII}]$ – $[^t\text{Bu}_3\text{PAuV}]$ narrow ranges for the electronic activation barriers are observed (4.8–6.1 kcal mol^{−1} range, see Table

S10†) and for the corresponding INT stabilization (−16.0/−18.4 kcal mol^{−1} range, see Table S11†), consistently with the very similar nature of the Au–Al bond described in the previous sections. This is further confirmed by investigating the nature of the interaction between CO₂ and complexes $[^t\text{Bu}_3\text{PAuI}]$ – $[^t\text{Bu}_3\text{PAuVI}]$ at both TSI and INT by relying on EDA-NOCV and CD approaches (the results are reported in Tables S12, S13, Fig. S16 and S17 in the ESI†). Unsurprisingly, the analysis reveals qualitative and quantitative analogies concerning the interactions taking place at TSI and INT in all cases. Indeed, consistently with the previously reported results for $[^t\text{Bu}_3\text{PAuI}]$ and $[^t\text{Bu}_3\text{PAuII}]$,^{33,45} in the first step of the reaction, each complex interacts with CO₂ mainly through a charge transfer from the electron-rich Au–Al bond (which behaves as a nucleophilic site) towards the LUMO of CO₂. The nature of this interaction can be clearly inferred by the isodensity pictures of the related NOCV deformation density ($\Delta\rho'_1$) in Fig. S16 and S17 in the ESI†. In addition, in all the cases, an inverse charge flux assists the reaction, namely the charge transfer from the HOMO of CO₂ towards the empty valence 3p_z orbital of Al (see isosurfaces $\Delta\rho'_1$ in Fig. S16 and S17 in the ESI†).

Despite these analogies, the ASM analysis reveals two outliers in the series, *i.e.* complexes $[^t\text{Bu}_3\text{PAuI}]$ and $[^t\text{Bu}_3\text{PAuVI}]$. For complex $[^t\text{Bu}_3\text{PAuI}]$, as shown in Fig. 6a and consistently with the free energy profiles reported in Fig. 4, the first step

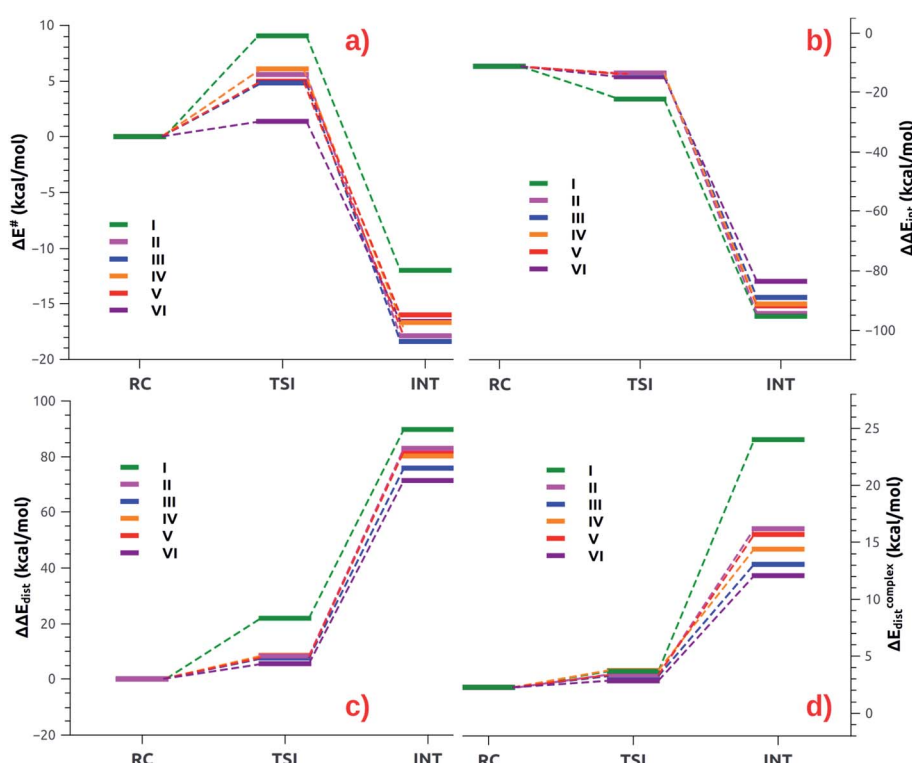


Fig. 6 (a) ASM diagrams for the electronic energy variation (ΔE) along the reaction path connecting RC, TSI and INT structures for complexes $[^t\text{Bu}_3\text{PAuI}]$ – $[^t\text{Bu}_3\text{PAuVI}]$. (b) ASM diagrams for the variation of the interaction energy stabilization ($\Delta\Delta E_{\text{int}}$) along the reaction path connecting RC, TSI and INT structures for complexes $[^t\text{Bu}_3\text{PAuI}]$ – $[^t\text{Bu}_3\text{PAuVI}]$. (c) ASM diagrams for the overall variation of the distortion energy penalty ($\Delta\Delta E_{\text{dist}}$) along the reaction path connecting RC, TSI and INT structures for complexes $[^t\text{Bu}_3\text{PAuI}]$ – $[^t\text{Bu}_3\text{PAuVI}]$. (d) ASM diagrams for the penalty due to the distortion of the complex ($\Delta E_{\text{complex}}$) along the reaction path connecting RC, TSI and INT structures for complexes $[^t\text{Bu}_3\text{PAuI}]$ – $[^t\text{Bu}_3\text{PAuVI}]$. Results for $[^t\text{Bu}_3\text{PAuI}]$ and $[^t\text{Bu}_3\text{PAuII}]$ have been taken from ref. 33 and 45, respectively.



features the highest activation barrier (10.9 and 9.0 kcal mol⁻¹ in terms of $\Delta G^\#$ and $\Delta E^\#$, respectively) and the least stable intermediate (-4.2 and -12.0 kcal mol⁻¹ in terms of ΔG and ΔE , respectively). By decomposing the reaction path we unravel that these differences mainly arise from an increased distortion penalty for [^tBu₃PAuI]: while overall $\Delta\Delta E_{\text{dist}}$ values for complexes [^tBu₃PAuII]-[^tBu₃PAuVI] at INT lie in a tight range (71.3–83.0 kcal mol⁻¹, Table S8†), [^tBu₃PAuI] reveals a higher distortion penalty along the path (89.9 kcal mol⁻¹), which, as it can be inferred from the results displayed in Fig. 6d, arises from a higher distortion of the complex when constrained at the INT geometry (ΔE_{dist} ^{complex} values lie in the 11.4/16.2 kcal mol⁻¹ range for complexes [^tBu₃PAuII]-[^tBu₃PAuVI], while the penalty associated with [^tBu₃PAuI] is 25.3 kcal mol⁻¹, Table S11†), consistently with [^tBu₃PAuI] displaying the longest (and thus most distorted from its equilibrium value) Au–Al bond (2.623 Å) at INT. Despite its flexibility, the highly sterically hindered (NON) ligand gets highly distorted at the strained geometry of INT, resulting in an increased distortion penalty.

On the other hand, complex [^tBu₃PAuVI] represents an outlier on the opposite side. It features the lowest activation barrier (0.5 and 1.4 kcal mol⁻¹ in terms of $\Delta G^\#$ and $\Delta E^\#$, respectively) and a very stable intermediate (-7.3 and -16.6 kcal mol⁻¹ in terms of ΔG and ΔE , respectively). In this case, as shown in Fig. 6b and c and from the data in Tables S10 and S11,† the increased stability arises from an enhanced ability of counterbalancing the distortion penalty with favorable and stabilizing interactions. By relying on the EDA results (Tables S12 and S13 in the ESI†), we can see that this enhanced stabilization mainly arises from a reduced Pauli repulsion at both TSI and INT, where such effect becomes very clear. Complexes [^tBu₃PAuI]-[^tBu₃PAuV] display ΔE_{Pauli} values at INT in the 406.2–384.2 kcal mol⁻¹ range, while complex [^tBu₃PAuVI] has a much lower associated ΔE_{Pauli} (356.8 kcal mol⁻¹). It is worth reminding that the decrease of Pauli repulsion has been found to be a stabilizing driving force in several catalytic processes involving organic substrates.⁵⁰ In this case, this stabilization, arising from a reduced two-orbital-four-electron repulsion, is mainly due to the reduced steric hindrance and smaller dimension of the aluminyll **VI**, which should help diminishing the filled orbitals' repulsion (see Tables S14–S18 and Fig. S18–S21† in the ESI for the effect of modelling **VI** with simplified substituents). It is clear that we are discussing very small differences in a reactivity that, overall, is very similar for all complexes. We also should note that the first step of the reaction is not the rate-determining step (RDS). However, this analysis suggests that the steric hindrance, rather than the electronic properties, of the aluminyll may represent a control factor on the reactivity of these species towards CO₂.

In the second step of the reaction, the oxygen atom of CO₂ attack to the electrophilic Al center requires higher activation free energy barriers than those for the nucleophilic attack to the CO₂ carbon atom, that, however, vary in a narrow range ($\Delta G^\#$ = 11.0/13.4 kcal mol⁻¹), and a stable product complex PC is formed for all the complexes. The TSII structures are all very similar (see Fig. S10–S15†) and the associated imaginary frequency is very small for all the complexes, indicating a very

flat potential energy surface involving the bending of the two [^tBu₃PAu] and [X] (X = **I**, **II**, **III**, **IV**, **V**, **VI**) fragments between which the CO₂ insertion occurs. Overall, the insertion products have very similar relative energies (in the range between -11.2 and -16.9 kcal mol⁻¹) and their stability can be related, as discussed in the previous works on [^tBu₃PAuI] and [^tBu₃PAuII],^{33,45} to a radical-like reactivity of the gold and aluminyll fragments that is able to stabilize the insertion product. Indeed, by analyzing the formation of the products starting from radical fragments (see Scheme S1 and Table S19 in the ESI†), we can clearly see that complexes [^tBu₃PAuI]-[^tBu₃PAuVI] have similarly stabilizing formation energies (ΔE in the range -106.0/-111.4 kcal mol⁻¹) from radical fragments, in accordance with the picture of a radical-like reactivity.

We also computed the extrusion of CO from the INT or PC complexes and it has revealed to be endergonic for all the anions: the resulting oxide complex [^tBu₃PAuOX] [CO] (X = **I**, **II**, **III**, **IV**, **V**, **VI**) has been calculated to be thermodynamically unstable with ΔG = 16.6, 14.9, 17.2, 16.9, 15.1 and 11.9 kcal mol⁻¹, respectively. This mechanistic perspective supports the picture described in the first section for this series of complexes, *i.e.* that no particularly remarkable reactivity difference between the considered gold-aluminyll complexes can be observed, coherently with the poor tunability of their electronic structure and bonding features.

The Au–Al bond nature/reactivity relationship observed here is fully consistent with the results previously found by us in ref. 45 for the CO₂ insertion reaction in gold-aluminyll (complex [^tBu₃PAuII]), -gallyl and -indyl complexes, where the highly covalent, low polarity Au–Al bond favors the reaction, whereas the increased polarity of the covalent Au(δ^+)-Ga(δ^-) and Au(δ^+)-In(δ^-) bonds makes these complexes weaker nucleophiles in a radical-like mechanism, which appears to be key to stabilize the CO₂ insertion product. Based on these findings, we expect that the different nature (which is mainly dative) of the Au–C bonds in carbene complexes with **I**^C, **II**^C, **III**^C, **IV**^C, **V**^C and **VI**^C ligands would impart a different reactivity with carbon dioxide. Although it is known that free NHCs can capture CO₂ to form the corresponding imidazolium carboxylates (featuring a C–CO₂ bond), examples of CO₂ insertion chemistry have been only reported for f-block M-NHC (M = Y, Ce, U) complexes, where the M-NHC bond is very weak and CO₂ can coordinate to NHC simply by displacing it from the metal.^{51–54} Indeed, in our case, the searching for INT- and PC-type structures using as an example complex [^tBu₃PAuII^C]⁺ failed, invariably leading to the highly unstable {[^tBu₃PAuCO][OCl(^{Si}NON)]}⁺ fragments, where CO₂ has been reduced to the CO coordinated to the gold fragment and the O atom coordinated to the carbene ligand (ΔG = 22.0 kcal mol⁻¹ above the separated reactants). Analogously, optimization of a PC structure, with the CO₂ carbon atom coordinated to the **II**^C C atom and one CO₂ oxygen atom coordinated to Au, gives a thermodynamically unstable product (ΔG = 20.3 kcal mol⁻¹ above the separated reactants), suggesting that an insertion of CO₂ into the Au–C bonds in the carbene complexes studied here is not thermodynamically feasible.



Conclusions

Based on the apparent alumanyl/carbene isolobal analogy, the possibility of tuning the features of the metal–alumanyl bond and its reactivity by imposing structural modifications on the alumanyl scaffold, similarly to what has been well established in carbene chemistry, has been explored in this work. Since in the case of gold, an Au–Al complex has been surprisingly shown to insert CO_2 at ambient conditions with a bimetallic radical-like reactivity, we have performed a comparative analysis of the electronic structure and reactivity of a series of gold-alumanyl complexes bearing experimentally characterized different alumanyl scaffolds to quantitatively assess this tunability.

The results very clearly demonstrate that alumynils are different from carbenes when used as coordination ligands to gold. Indeed, while the Au–C bond in Au(i)-NHC complexes has been proven to be of a dative nature and electronically highly tunable through NHC structure modification, all the alumanyl complexes under investigation feature an electron-sharing, weakly polarized Au–Al bond which is poorly influenced by the structural variations of the ligand scaffold.

The computed CO_2 reaction mechanisms for the series of gold-alumanyl complexes clearly reflect the scarce tunability of the Au–Al bond in the series. Indeed, the computed reaction profiles are highly similar from both a qualitative and quantitative perspective. In all the cases, the insertion of CO_2 into the Au–Al bond features a bimetallic radical-like reactivity, with the Au–Al bond being the nucleophilic site and the vacant $3p_z$ orbital of Al assisting as an electrophilic site. In addition, despite some differences that can be explained in terms of steric hindrance of the alumanyl ligand, the two reaction steps (namely, the Au–Al nucleophilic attack to CO_2 and CO_2 attack to electrophilic Al) feature activation barriers of comparable amount and similarly stabilized intermediates/products, highlighting that this reactivity is poorly controlled by electronic effects associated with the different geometrical arrangement of the alumanyl scaffold, which is in line with recent experimental evidence.⁶⁵

We mention that, although the nature of the M–Al bonds in X-type PAIP pincer alumanyl complexes and their reactivity have recently been the subject of several works,^{66–69} a study of the effect of systematic structural modifications of the monodentate anionic alumanyl (**I**) scaffold on the M–Al bond features and complexes reactivity was still lacking in the literature.

This work fits in the currently expanding literature concerning the alumanyl anions, exploiting their peculiar behavior when used as coordination ligands and it also fits in the framework of ligand design of efficient transition-metal-alumanyl complexes for the CO_2 capture.

Computational details

Alumanyl anions **I**–**VI** have been slightly simplified as follows: **I** by replacing the two *tert*-butyl groups at the peripheral positions of the dimethylxanthene moiety with hydrogen atoms and the two Dipp substituents on the nitrogen atoms with phenyl groups (denoted as NON'); **II**, **III** and **IV** by replacing the two

Dipp substituents on the nitrogen atoms with phenyl groups (denoted as $^{\text{Si}}\text{NON}'$, NCCN' and $^{\text{Dipp}}\text{BDI-H}'$, respectively); **V** and **VI** by replacing the methyl groups at the Si by hydrogen atoms (denoted as CAA' and $\{\text{C}(\text{SiH}_3)_2\text{CH}_2\}_2$, respectively). The same modelling of the NON fragment has been used in ref. 33 and it has been shown to give good agreement with available experimental geometrical data for complex $[\text{Bu}_3\text{PAuI}]$. The effect of modelling **I**–**VI** with simplified substituents on the gold complexes reaction mechanism and electronic structure calculations has been quantitatively evaluated by using gold complex with **VI** (and the corresponding stationary points) as test case. As shown in Tables S14–S18 and Fig. S18–S21 in the ESI,[†] effects of the simplifications are found which are mainly associated with the modified (decreased) steric hindrance of the alumanyl ligand. The modelling of the alumanyl ligands negligibly affects the electronic structure results and the chemical insight presented here, while allowing to reduce the computational cost. Geometry optimizations and frequency calculations of free **I**–**VI**, **I**^C–**VI**^C ligands and corresponding gold complexes and related minima and transition states for each reaction path (minima with zero imaginary frequencies and transition states with one imaginary frequency) have been carried out using the Amsterdam Density Functional (ADF) code^{55,56} in combination with the related Quantum-regions Interconnected by Local Description (QUILD) program.⁵⁷ The PBE⁵⁸ GGA exchange-correlation (XC) functional, the TZ2P basis set with a small frozen core approximation for all atoms, the ZORA Hamiltonian^{59–61} for treating scalar relativistic effects and the Grimme's D3-BJ dispersion correction were used.^{62,63} Solvent effects were modeled employing the Conductor-like Screening Model (COSMO) with the default parameters for toluene as implemented in the ADF code.⁶⁴ The same computational setup has also been used for the EDA, CD-NOCV,⁴¹ and AMS calculations and for computing the radical reactions between [X], $[\text{CO}_2]$ and $[\text{Bu}_3\text{PAu}]$ fragments. EDA, ETS-NOCV and CD-NOCV calculations have been carried out in gas phase, since inclusion of implicit solvation has no effect on their results (see Table S20 and Fig. S22 in the ESI[†]). This protocol has been used successfully in ref. 33 and 45 to study the $[\text{Bu}_3\text{PAuAl}(\text{NON})]$ and $[\text{Bu}_3\text{PAuCO}_2\text{Al}(\text{NON})]$ complexes. The PBE performance has been tested by comparison with results obtained using the hybrid PBE0 functional (see Tables S21–S23, Fig. S23 and S24 in the ESI[†]). For further details and description of the methods used in this work, see the Methodology section in the ESI.[†]

Data availability

All the relevant data (including methodology description, mechanistic, CD-NOCV, AMS and EDA data discussed in the manuscript) are provided within the ESI.[†]

Author contributions

D. S., L. B. and P. B. conceived the project, D. S., L. B. and P. B. performed the research, D. S., L. B. and P. B. wrote the manuscript.



Conflicts of interest

The authors declare no competing financial interests.

Acknowledgements

All the authors gratefully acknowledge the funding support from Ministero dell'Università e della Ricerca (MUR, project AMIS, through the program “Dipartimenti di Eccellenza – 2018–2022”) and P. B. from University of Perugia (“Fondo Ricerca di Base 2019”).

Notes and references

- J. Hicks, P. Vasko, J. M. Goicoechea and S. Aldridge, *Nature*, 2018, **557**, 92–95.
- J. Hicks, P. Vasko, J. M. Goicoechea and S. Aldridge, *J. Am. Chem. Soc.*, 2019, **141**, 11000–11003.
- R. J. Schwamm, M. D. Anker, M. Lein and M. P. Coles, *Angew. Chem., Int. Ed.*, 2019, **58**, 1489–1493.
- R. J. Schwamm, M. P. Coles, M. S. Hill, M. F. Mahon, C. L. McMullin, N. A. Rajabi and A. S. S. Wilson, *Angew. Chem.*, 2020, **132**, 3956–3960.
- S. Grams, J. Eyselein, J. Langer, C. Färber and S. Harder, *Angew. Chem.*, 2020, **132**, 16116–16120.
- S. Kurumada, S. Takamori and M. Yamashita, *Nat. Chem.*, 2020, **12**, 36–39.
- K. Koshino and R. Kinjo, *J. Am. Chem. Soc.*, 2020, **142**, 9057–9062.
- J. Hicks, P. Vasko, J. M. Goicoechea and S. Aldridge, *Angew. Chem., Int. Ed.*, 2021, **60**, 1702–1713.
- S. Díez-González, N. Marion and S. P. Nolan, *Chem. Rev.*, 2009, **109**, 3612–3676.
- H. Jacobsen, A. Correa, A. Poater, C. Costabile and L. Cavallo, *Coord. Chem. Rev.*, 2009, **253**, 687–703.
- The organometallic chemistry of N-heterocyclic carbenes*, H. V. Huynh, John Wiley & Sons, Ltd, Chichester, UK, 2017.
- F. E. Hahn, M. C. Jahnke, F. E. Hahn and M. C. Jahnke, *Angew. Chem., Int. Ed.*, 2008, **47**, 3122–3172.
- M. N. Hopkinson, C. Richter, M. Schedler and F. Glorius, *Nature*, 2014, **510**, 485–496.
- D. J. Nelson and S. P. Nolan, *Chem. Soc. Rev.*, 2013, **42**, 6723–6753.
- H. V. Huynh, *Chem. Rev.*, 2018, **118**, 9457–9492.
- D. Bourissou, O. Guerret, F. P. Gabbaï and G. Bertrand, *Chem. Rev.*, 1999, **100**, 39–91.
- J. Li, W. Shen and X. Li, *Curr. Org. Chem.*, 2012, **16**, 2879–2891.
- L. García, K. H. M. Al Furajji, D. J. D. Wilson, J. L. Dutton, M. S. Hill and M. F. Mahon, *Dalton Trans.*, 2017, **46**, 12015–12018.
- D. M. Andrada, N. Holzmann, T. Hamadi and G. Frenking, *Beilstein J. Org. Chem.*, 2015, **11**, 2727–2736.
- D. Martin, N. Lassauque, B. Donnadieu and G. Bertrand, *Angew. Chem., Int. Ed.*, 2012, **51**, 6172–6175.
- V. Lavallo, Y. Canac, C. Präsang, B. Donnadieu and G. Bertrand, *Angew. Chem., Int. Ed.*, 2005, **44**, 5705–5709.
- M. Soleilhavoup and G. Bertrand, *Acc. Chem. Res.*, 2014, **48**, 256–266.
- S. Roy, K. C. Mondal and H. W. Roesky, *Acc. Chem. Res.*, 2016, **49**, 357–369.
- A. Sundermann, M. Reiher and W. W. Schoeller, *Eur. J. Inorg. Chem.*, 1998, **1998**, 305–310.
- H. Jacobsen, A. Correa, C. Costabile and L. Cavallo, *J. Organomet. Chem.*, 2006, **691**, 4350–4358.
- X. Hu, I. Castro-Rodriguez, K. Olsen and K. Meyer, *Organometallics*, 2004, **23**, 755–764.
- D. M. Khramov, V. M. Lynch and C. W. Bielawski, *Organometallics*, 2007, **26**, 6042–6049.
- R. J. Harris and R. A. Widenhoefer, *Chem. Soc. Rev.*, 2016, **45**, 4533–4551.
- D. Marchione, L. Belpassi, G. Bistoni, A. Macchioni, F. Tarantelli and D. Zuccaccia, *Organometallics*, 2014, **33**, 4200–4208.
- C. A. Gaggioli, G. Bistoni, G. Ciancaleoni, F. Tarantelli, L. Belpassi and P. Belanzoni, *Chem. –Eur. J.*, 2017, **23**, 7558–7569.
- D. Sorbelli, P. Belanzoni and L. Belpassi, *Eur. J. Inorg. Chem.*, 2021, **2021**, 2401–2416.
- J. Hicks, A. Mansikkämäki, P. Vasko, J. M. Goicoechea and S. Aldridge, *Nat. Chem.*, 2019, **11**, 237–241.
- D. Sorbelli, L. Belpassi and P. Belanzoni, *J. Am. Chem. Soc.*, 2021, **143**, 14433–14437.
- M. J. Evans, M. D. Anker and M. P. Coles, *Inorg. Chem.*, 2021, **60**, 4772–4778.
- J. J. Dunsford, K. J. Cavell and B. M. Kariuki, *Organometallics*, 2012, **31**, 4118–4121.
- M. Cybularczyk-Cecotka, A. M. Dabrowska, P. A. Guńka and P. Horeglad, *Inorganics*, 2018, **6**(28), 28.
- T. Ziegler and A. Rauk, *Theor. Chim. Acta*, 1977, **46**, 1–10.
- K. Morokuma, *J. Chem. Phys.*, 1971, **55**, 1236–1244.
- L. Belpassi, I. Infante, F. Tarantelli and L. Visscher, *J. Am. Chem. Soc.*, 2008, **130**, 1048–1060.
- G. Bistoni, S. Rampino, F. Tarantelli and L. Belpassi, *J. Chem. Phys.*, 2015, **142**, 084112.
- GitHub – BERTHA-4c-DKS/pycubescd*, <https://github.com/BERTHA-4c-DKS/pycubescd>.
- M. P. Mitoraj, A. Michalak and T. Ziegler, *J. Chem. Theory Comput.*, 2009, **5**, 962–975.
- L. Zhao, M. von Hopffgarten, D. M. Andrada and G. Frenking, *Wiley Interdiscip. Rev. Comput. Mol. Sci.*, 2018, **8**, e1345.
- P. Jerabek, P. Schwerdtfeger and G. Frenking, *J. Comput. Chem.*, 2019, **40**, 247–264.
- D. Sorbelli, L. Belpassi and P. Belanzoni, *Inorg. Chem.*, 2022, **61**, 1704–1716.
- D. Marchione, L. Belpassi, G. Bistoni, A. Macchioni, F. Tarantelli and D. Zuccaccia, *Organometallics*, 2014, **33**, 4200–4208.
- I. Ferná and F. M. Bickelhaupt, *Chem. Soc. Rev.*, 2014, **43**, 4953.
- F. M. Bickelhaupt and K. N. Houk, *Angew. Chem., Int. Ed.*, 2017, **56**, 10070–10086.



49 P. Vermeeren, S. C. C. van der Lubbe, C. Fonseca Guerra, F. M. Bickelhaupt and T. A. Hamlin, *Nat. Protoc.*, 2020, **15**, 649–667.

50 T. A. Hamlin, F. M. Bickelhaupt and I. Fernández, *Acc. Chem. Res.*, 2021, **54**, 1972–1981.

51 L. Yang and H. Wang, *ChemSusChem*, 2014, **7**, 962–998.

52 P. L. Arnold, R. W. F. Kerr, C. Weetman, S. R. Docherty, J. Rieb, F. L. Cruickshank, K. Wang, C. Jandl, M. W. McMullon, A. Pöthig, F. E. Kühn and A. D. Smith, *Chem. Sci.*, 2018, **9**, 8035–8045.

53 P. L. Arnold, Z. R. Turner, A. I. Germeroth, I. J. Casely, G. S. Nichol, R. Bellabarba and R. P. Tooze, *Dalton Trans.*, 2013, **42**, 1333–1337.

54 P. L. Arnold, I. A. Marr, S. Zlatogorsky, R. Bellabarba and R. P. Tooze, *Dalton Trans.*, 2013, **43**, 34–37.

55 E. J. Baerends, T. Ziegler, J. Autschbach, D. Bashford, A. Bérces, F. M. Bickelhaupt, C. Bo, P. M. Boerrigter, L. Cavallo, D. P. Chong, L. Deng, R. M. Dickson, D. E. Ellis, M. van Faassen, L. Fan, T. H. Fischer, C. Fonseca Guerra, M. Franchini, A. Ghysels, A. Giannonna, S. J. A. van Gisbergen, A. W. Götz, J. A. Groeneveld, O. V. Gritsenko, M. Grüning, S. Gusarov, F. E. Harris, P. van den Hoek, H. Jacobsen, L. Jensen, J. W. Kaminski, G. van Kessel, F. Kootstra, A. Kovalenko, M. V. Krykunov, E. van Lenthe, D. A. McCormack, A. Michalak, M. Mitoraj, S. M. Morton, J. Neugebauer, V. P. Nicu, L. Noddleman, V. P. Osinga, S. Patchkovskii, M. Pavanello, P. H. T. Philipsen, D. Post, C. C. Pye, W. Ravenek, J. I. Rodríguez, P. Ros, P. R. T. Schipper, H. van Schoot, G. Schreckenbach, J. S. Seldenthuis, M. Seth, J. G. Snijders, M. Solà, M. Swart, D. Swerhone, G. te Velde, P. Vernooij, L. Versluis, L. Visscher, O. Visser, F. Wang, T. A. Wesolowski, E. M. van Wezenbeek, G. Wiesenecker, S. K. Wolff, T. K. Woo and A. L. Yakovlev, *ADF2014, SCM, Theoretical Chemistry*, Vrije Universiteit, Amsterdam, The Netherlands, <https://www.scm.com>.

56 G. te Velde, F. M. Bickelhaupt, E. J. Baerends, C. Fonseca Guerra, S. J. A. van Gisbergen, J. G. Snijders and T. Ziegler, *J. Comput. Chem.*, 2001, **22**, 931–967.

57 M. Swart and F. M. Bickelhaupt, *J. Comput. Chem.*, 2008, **29**, 724–734.

58 J. P. Perdew, K. Burke and M. Ernzerhof, *Phys. Rev. Lett.*, 1996, **77**, 3865–3868.

59 E. Van Lenthe, E. J. Baerends and J. G. Snijders, *J. Chem. Phys.*, 1993, **99**, 4597–4610.

60 E. Van Lenthe, E. J. Baerends and J. G. Snijders, *J. Chem. Phys.*, 1994, **101**, 9783–9792.

61 E. Van Lenthe, *J. Chem. Phys.*, 1999, **110**, 8943–8953.

62 S. Grimme, J. Antony, S. Ehrlich and H. Krieg, *J. Chem. Phys.*, 2010, **132**, 154104.

63 S. Grimme, S. Ehrlich and L. Goerigk, *J. Comput. Chem.*, 2011, **32**, 1456–1465.

64 C. C. Pye and T. Ziegler, *Theor. Chem. Acc.*, 1999, **101**, 396–408.

65 H.-Y. Liu, S. E. Neale, M. S. Hill, M. F. Mahon and C. L. McMullin, *Dalton Trans.*, 2022, **51**, 3913–3924. This work has been published during the revision of the present manuscript. The authors study the experimental reactivity of different coinage metal (Cu, Ag, Au) complexes bearing aluminyls **I** and **II** with carbon dioxide and *N,N'*-diisopropylcarbodiimide, finding no significant difference in the reactivity.

66 N. Kuriakose, J.-J. Zheng, T. Saito, N. Hara, Y. Nakao and S. Sakaki, *Inorg. Chem.*, 2019, **58**, 4894–4906.

67 N. Hara, K. Yamamoto, Y. Tanaka, T. Saito, S. Sakaki and Y. Nakao, *Bull. Chem. Soc. Jpn.*, 2021, **94**, 1859–1868.

68 J. Takaya and N. Iwasawa, *J. Am. Chem. Soc.*, 2017, **139**, 6074–6077.

69 Q.-Z. Li, N. Hara, K. Semba, Y. Nakao and S. Sakaki, *Top. Catal.*, 2022, **65**, 392–417.

